Journal of Highway and Transportation Research and Development
2024,18(2):26-33
ISSN 2095-6215
DOI: 10.26599/HTRD.2024.9480011

# Curb Detection and Mapping via Robust Iterative Gaussian Process Regression

Di Wang[*1§], Si Chen[2§], Zhenni Ma[1§], Jiajia Shi[1], Fuchun Zhang[**1]

(1. School of Physics and Electronic Information, Yan'an University, Yan'an, Shaanxi 716000, China;
2. China Electronics Technology Group Corporation, Beijing 100086, China)

**Abstract**: Curb detection and mapping are of great importance to ensure the safety and efficiency of intelligent vehicles. However, it remains challenging because shape estimation under noise and outliers is not well addressed in real traffic scenarios. In this paper, an efficient curb detection and mapping algorithm is proposed to achieve an accurate representation of curb shape. More specifically, an iterative Gaussian process regression (iGPR) is introduced, where each candidate point is verified multiple times. Then iGPR is employed in shape estimation of both road profile and curb, which serves as the backbone unit in curb candidate detection. During this process, the input 3D point cloud is segmented into road and obstacles, and potential curb points are selected by evaluating physically interpretable curb features. Finally, the proposed iGPR is validated and tested on two large-scale, complex urban datasets under real traffic scenarios. Experimental results show that the proposed iGPR achieves better performance than several state-of-the-art algorithms.

**Key words**: road engineering; shape estimation; curb mapping; gaussian process regression; iGPR; autonomous driving

## 1 Introduction

Curb detection and mapping served as crucial physical barrier in urban scenarios, Perception and planning tasks by defining drivable areas or region of interest[1-3]. However, it remains a challenging problem, especially in large-scale and complex urban environments.

On one hand, selecting reliable, stable, and precise curb candidate points from 3D point clouds is difficult due to the limited spatial resolution or sparsity of input point clouds and flexible characteristics pertaining to the curb[4-5]. On the other hand, finding an appropriate shape model that guarantees booth flexibility and accuracy poses a great challenge for curb mapping. Though there exists a plethora of shape models consisting of point set[6], polynomials[7], clothoids[8] and spline[9] developed during the last decades, the drawbacks of these shape models are obvious, i. e., the parameter tuning involved are problematic when applied in the large-scale area and approximating accuracies can be degraded when the portion of noise and outliers is unavoidable.

In this paper, a precise and robust iterative Gaussian process regression (iGPR) based curb detection and mapping algorithm is proposed. Compared with the original work[8], there exist three major improvements.

A robust iterative Gaussian process regression for the shape estimation of road profile and curb is introduced.

An accurate curb detection and mapping algorithm combined with road segmentation and distinctive curb feature selection is proposed.

Extensive experiments are conducted on two large-scale and complex urban scenario datasets which are captured in real traffic flow, and the results show that the proposed algorithm achieves better performance over several state-of-art algorithms.

The remainder of this paper is organized as follows. Section 2 introduces the core shape estimation algorithm iGPR, and Section 3 presents reliable road profile estimation and curb feature selection. Section 4 tets validated the proposed algorithm on two large-scale and complex dataset. Finally, conclusions and future work are discussed in Section 5.

Received 14 September 2023; Revised 22 December 2023; Accepted 30 December 2023

[*] *E-mail address*: 280868861@qq.com; [§] Di Wang, Si Chen, and Zhenni Ma are co-first authors

[**] Corresponding author, yadxzfc@yau.edu.cn

## 2 Iterative gaussian process regression

As illustrated in Figure 1, the core of curb detection and mapping lies in road shape model, which iteratively estimates outlier and road shape in Figure 2.

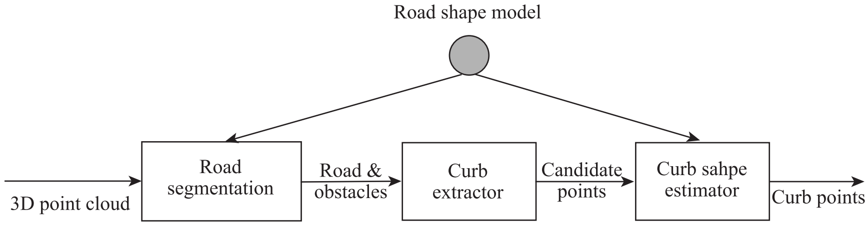


**Fig. 1 Curb detection and mapping pipeline**

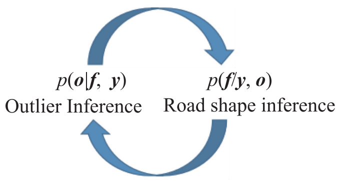


**Fig. 2 Iterative GPR pipeline**

### 2.1 Problem formulation

Given a 2D point set $\boldsymbol{P} = \{x_i, y_i\}_{i=1,2,\cdots,NP} = \{\boldsymbol{p}_i\}_{i=1,2,\cdots,NP} = \{x, y\}$, $\boldsymbol{x}, \boldsymbol{y} \in \mathbb{R}$ $\boldsymbol{p}_i \in \mathbb{R}^2$, $x, y \in \mathbb{R}^{NP}$, our task is to estimate a precise and smooth shape for road profile or curbs as well as detect the potential outliers.

$$y_i = f(x_i) + \varepsilon, \tag{1}$$

where $f(x_i)$ denotes a smooth curve and $\varepsilon$ denotes noise.

In our previous work[10], the smooth curve in Equation(1) is assumed to be drawn from a Gaussian process (GP), and an iterative Gaussian process regression (iGPR) is proposed to gradually eliminate and suppress the outliers and noise respectively.

The main task can be formulated as follows: given an initial training set $\boldsymbol{T} = \{x_i, y_i\}_{i=1,2,\cdots,NT=\{\hat{x},\hat{y}\}}$ and test set $\boldsymbol{V} = \{x_{i*}, y_{i*}\}_{i=1,2,\cdots,Nv} = \{\boldsymbol{x}_*, \boldsymbol{y}_*\}$, the shape is gradually estimated by GPR with the gradually refined $\boldsymbol{T}$ and $\boldsymbol{V}$. The details of the algorithm are as follows.

Since the curve represented by iGPR in Equation (1) has the formula $y=f(x)$, it is problematic when the curve is in the vertical direction, i.e. $x=f(y)$. Therefore, the input data $\boldsymbol{P}$ is required to be transformed towards a horizontal direction before applying iGPR. The transformation $(\boldsymbol{R}, \boldsymbol{t}) \in SE(3)$ is computed by principle component analysis ($\boldsymbol{P}_{CA}$).

$$\boldsymbol{R} = P_{CA}\left(\sum_{i=1}^{N} \boldsymbol{p}_i \boldsymbol{p}_i^{\mathrm{T}}\right) \tag{2}$$

$$\boldsymbol{t} = \frac{1}{N}\sum_{i=1}^{N} \boldsymbol{p}_i. \tag{3}$$

### 2.2 Road shape inference

The road shape in Equation(1) can be modeled by a Gaussian process

$$f(x) = \mathrm{GP}[\boldsymbol{m}(x), k(x, x')], \tag{4}$$

where, $\boldsymbol{m}(x)$ is the mean function and is set to be zero for simplicity; $k(x, x') \geqslant 0$ is the covariance function specified by users.

#### 2.2.1 Gaussian process posterior

The Gaussian process states that the training set $\boldsymbol{T}$ and the test set $\boldsymbol{V}$ are joint Gaussian distributions, thus the posterior probabilistic distribution of $\boldsymbol{V}$ is also a Gaussian distribution

$$p(\boldsymbol{y}_* \mid \hat{\boldsymbol{y}}, \hat{\boldsymbol{x}}, \boldsymbol{x}_*) \sim N(\boldsymbol{m}_*, C_*), \tag{5}$$

where it's mean and covariance can be computed[11]

$$\boldsymbol{m}_* = \boldsymbol{K}_* \boldsymbol{K}^{-1} \hat{\boldsymbol{Y}}, \tag{6}$$

$$\boldsymbol{C}_* = \boldsymbol{K}_{**} - \boldsymbol{K}_* \boldsymbol{K}^{-1} \boldsymbol{K}_*^{\mathrm{T}}, \tag{7}$$

where, $\boldsymbol{K} \in \mathbb{R}^{NT\times NT}$, $\boldsymbol{K}_* \in \mathbb{R}^{NV\times NP}$, and $\boldsymbol{K}_{**} \in \mathbb{R}^{NV\times NV}$ are covariance matrices computed via covariance function $k(x, x')$. $\boldsymbol{m}_* \in \mathbb{R}^{NV}$ and $\boldsymbol{C}_{**} \in \mathbb{R}^{NV\times NV}$ are predicted mean and covariance matrices. In this paper, the covariance function is set to be the squared exponential kernel function

$$k(x, x') = \delta_f^2 \exp\left[-\frac{(x - x')^2}{2l^2}\right] + \delta_n^2 \delta(x, x'), \tag{8}$$

where, $\delta(x, x')$ denotes the Kronecker delta function; and $l$ denotes the characteristic length of $k(x, x')$. With given training data, the hyper-parameters $\boldsymbol{\theta} = \{\delta_f, \delta_n, l\}$ can be learned via the gradient descent (GD) method.

#### 2.2.2 Hyperparameter learning

The hyper-parameters $\boldsymbol{\theta}$ can be learned[11] by maximizing the logarithm of marginal likelihood, girven the training set $\boldsymbol{T}$:

$$\ln p(\hat{y}\mid\hat{x},\theta) = -\frac{1}{2}\hat{Y}^{\mathrm{T}}K^{-1}\hat{Y} - \frac{1}{2}\ln\mid K\mid, \tag{9}$$

where $\ln(\cdot)$ is the nature logrithm.

To speed up the learning process, the quasi-Newton method like Broyden-Fletcher-Goldfarb-Shanno (BFGS) is employed.

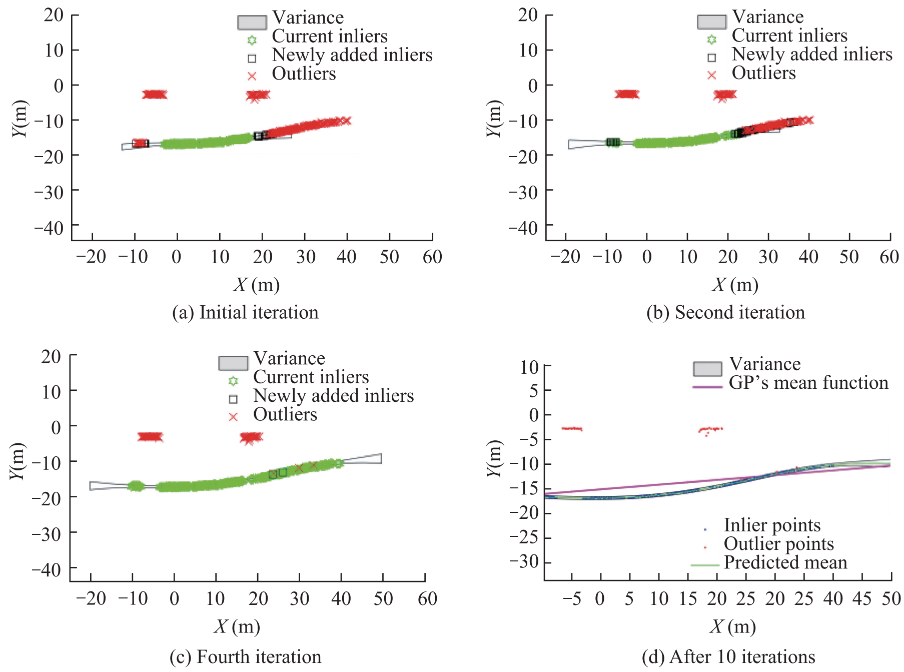

(a) Initial iteration (b) Second iteration (c) Fourth iteration (d) After 10 iterations

**Fig. 3 iGPR for road shape estimation**

### 2.2.3 Reducing inference time

Since the complexity of matrix inverse in Equation (6), (7), (9) is $O(N_T^3)$, the cardinality of the training set $\boldsymbol{T}$ should be as small as possible in order to speed up the learning and inference process. Therefore, the sparse support vector (SSV) $\boldsymbol{T}^{\mathrm{sp}}$ is proposed to reduce the computational complexity.

To attain SSV, a regular lattice grid with resolution $\boldsymbol{L}_S$ is firstly imposed on the input training set $\boldsymbol{T}_{r-1}$, then the centroid point of each individual non-empty grid can be easily computed by averaging the points within it, and the resulting centroid points is denoted as $\boldsymbol{G}$. Lastly, the SSV $\boldsymbol{T}^{\mathrm{sp}}$ is attained by performing the nearest neighbor search (NNS) from $\boldsymbol{G}$ against $\boldsymbol{T}_{r-1}$.

## 2.3 Outlier inference

After attaining the hyper-parameter $\boldsymbol{\theta}$ and SSV $\boldsymbol{T}^{\mathrm{sp}}$, a test set is constructed. The idea behind it is to spare the computational efforts, i.e., only points near the SSV $\boldsymbol{T}^{\mathrm{sp}}$ are incorporated into the test set $\boldsymbol{T}$, i.e.,

$$\boldsymbol{V}_r = \{\boldsymbol{p}_i \mid \boldsymbol{p}_i \in \boldsymbol{P}, \boldsymbol{p}_x - \boldsymbol{t}_0 \leqslant \boldsymbol{l}_e \mid\mid \boldsymbol{t}_1 - \boldsymbol{p}_x \geqslant \boldsymbol{l}_e\}. \tag{10}$$

where $\boldsymbol{T}_0$ and $\boldsymbol{T}_1$ denote the maximal and minimal $x$ value of sparse support vector, respectively. Consequently, each individual point in $\boldsymbol{V}_{\mathrm{r}}$ is classified as an inlier point using the following criteria[12]

$$\boldsymbol{C}_{ii*} \leqslant t_{\mathrm{m}}, \tag{11}$$

$$\frac{|\boldsymbol{y}_{i*} - \boldsymbol{m}_{i*}|}{\sqrt{\boldsymbol{C}_{ii*}}} \leqslant \boldsymbol{t}_{\mathrm{d}}, \tag{12}$$

where $t_m$ and $t_d$ are manually set thresholds. An example of iGPR for road shape estimation is illustrated in Figure 3, where the road shape is gradually recovered in an iterative manner. All outlier points are eliminated. The initial training set is selected via DBSCAN

The remaining challenge lies in how to select the initial training set $T_0$, and it is closely related to the prior knowledge on the shape of $\boldsymbol{P}$. We will cover them in the following sections.

# 3 Curb candidates detection

To reliably detect the curb candidates, a precise road profile model (RPM) is the first step and it is often ignored or simplified as a planar or linear shape, which often fails in complex urban scenarios. Also, the features pertaining to the curb are required to be precise, stable, and robust.

### 3.1 3D point cloud

The 3D point cloud is captured from widely deployed 3D LiDAR sensor Velodyne HDL-64E, which is consisted of 64 laser emitters and outputs millions of points per second.

#### 3.1.1 Ring structure

The advantage of HDL-64E is that its output 3D point cloud is naturally structured as several rings, namely, $\boldsymbol{H}=\{\boldsymbol{R}_i\}_{i=1,2,\cdots,NH}$ denotes one frame of the point cloud, $\boldsymbol{R}_i=\{\boldsymbol{p}_{ij}\}_{j=1,2,\cdots,Ni}$, where $\boldsymbol{p}_{ij}\in R^3$ denotes a 3D point and $i$ denotes the layer index, $j$ denotes the point index which sorts the points with ascending azimuth angle.

#### 3.1.2 Polar coordinate spatial partition

Unlike lattice coordinate-based occupancy grid map, the polar coordinate-based occupancy grid map partitions the 3D space using specific radius array $\boldsymbol{r}=\{r_i\}_{i=1,2,\cdots,Nr}$ and azimuth angle array $\boldsymbol{\theta}=\{\theta_i\}_{i=1,2,\cdots,N\theta}$. Afterward, a bunch of fan-shaped sectors is generated and can be efficiently retrieved and processed by the index of radius and angle. Specifically, a 3D point denoted with $\boldsymbol{p}_{ij}=(x,y,z)$ is assigned to a fan-shaped sector $\boldsymbol{F}_{mn}$ if it satisfies

$$\theta_m\leqslant\tan^{-1}(y,x)<\theta_{m+1}, \tag{13}$$

$$r_n\leqslant\sqrt{x^2+y^2}<r_{n+1}, \tag{14}$$

where $m$ and $n$ are the index of angle and radius, respectively.

Sectors pertaining to the same angle index constitute a segment $\boldsymbol{S}_m=\{\boldsymbol{F}_{mn}\}_{n=1,2,\cdots,Nr}$.

### 3.2 iGPR-based road profile modelling

The main idea of RPM is to model the road surface in each segment with a smooth and precise curve, and iGPR is employed in this paper. As illustrated in Figure 4, the proposed iGPR can divide the 3D point cloud into road and obstacle.

#### 3.2.1 Generating the input of iGPR

For each individual segment $\boldsymbol{S}_m$, the required input to iGPR is a 2D point set $\boldsymbol{P}_m$. For each non-empty sector, $\boldsymbol{F}_{mn}$, a potential road point $\boldsymbol{p}^{\mathrm{S}}_{mn}=(x,y,z)\in\mathbb{R}^3$ is selected by finding the point with the lowest height value, then $\boldsymbol{p}_{mn}=(\sqrt{x^2+y^2},z)\in\boldsymbol{R}^2$ is computed and incorporated into $\boldsymbol{P}_m$.

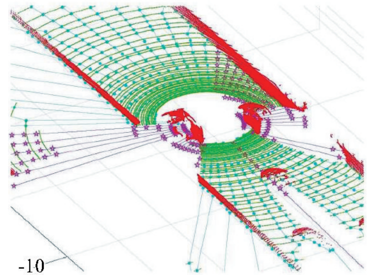


**Fig. 4 Road segmentation via iGPR**

#### 3.2.2 Selecting the initial training Set

To attain the initial training set, a linear model is employed for $\boldsymbol{P}_m$ to coarsely extract the reliable road points

$$(k,b)^*=\operatorname{argmin}\sum_{i=1}^{Nr}g_\sigma(kx_i+b-z_i), \tag{15}$$

where, $(k,b)^*$ is the line parameter; $g_\sigma(\cdot)$ is Huber loss.

#### 3.2.3 Validating physically feasible RPM

The iGPR-based curve can be learned via iGPR given the initial training set $\boldsymbol{T}_0$, and the road height $z$ for arbitrary radius can be easily inferred from Equation (6). However, it should bear in mind that not every segment can generate a physically feasible road surface model. Due to the unavoidable occlusion, the point number of $\boldsymbol{P}_m$ may be too few to infer a reliable road profile model, or the initial training set $\boldsymbol{T}_0$ may be erroneous when the moderate portion of the point cloud is sampled from other traffic participators.

To overcome the aforementioned problems, the physical constraint is introduced to validate each segment's resulting road surface model, i.e., the road height near the vehicle's front/rear tire is constrained by the external calibration between LiDAR and the host vehicle. Particularly, assuming the predicted height for the position of the front/rear tire is $z_{\mathrm{GP}}$, and the installation height of LiDAR denotes $z_{\mathrm{HDL}}$, the following constraint should be obeyed

$$|z_{\mathrm{GP}}-z_{\mathrm{HDL}}|\leqslant l_{\mathrm{g}}, \tag{16}$$

where $l_{\mathrm{g}}$ is a manually set threshold. If the iGPR-induced curve cannot satisfy Equation (16), the segment it belongs to is labeled with the undetermined segment.

#### 3.2.4 Classifying points in sector

For each non-empty sector $\boldsymbol{S}_{mn}$, the points within it are classified into road and obstacle according to respective iGPR-based RPM. For simplicity, the road surface of each sector is assumed to be a unitary plane, and the height of the plane or road height is computed from RPM. As mentioned in the aforementioned subsection, all the segments can be classified as segments possessing reliable RPM and undetermined segments. Consequently, the road height can be directly read from RPM when the corresponding sector $\boldsymbol{S}_{mn}$ belongs to segments possessing reliable RPM.

For a sector belonging to undetermined segments, its road height is computed by averaging the neighboring road height drawn from reliable RPM. The process of neighboring search is carefully designed, i. e., the search radius is from small to large until the number of neighboring road heights is moderate.

#### 3.2.5 Other considerations

To speed up the iGPR-based RPM, the hyper-parameter learning is disabled and $\boldsymbol{\theta}$ are pre-trained and applied to all the segments to save the computational resource. Also, since $\boldsymbol{P}_m$ in each segment is already sparse with proper radius array $\boldsymbol{r}$, box filter is dropped out.

### 3.3 Curb candidates selector

The intuitive behind the curb candidates selection is that curb candidates have distinctive geometric and semantic characteristics compared with other obstacles.

➢ The curb candidate point is the connecting point that reliably delineates the road and obstacles. Here "reliably" means both the number of points belonging to the road and the obstacle is enough.

➢ The curb candidate point is almost clung to the road surface.

➢ The curb candidate point is near the host vehicle.

#### 3.3.1 Layer-wise input

The curb candidates selector is employed in a layer-wise sequence. Consider one layer of points $\boldsymbol{R}_i = \{p_{ij}, s_{ij}\}_{j=1,2,\cdots,NH}$, where $i$ is the layer ID, $s_{ij}$ is road/obstacle labels.

#### 3.3.2 Semantic cluster

At first, the cluster is initial with an empty set. The searching process starts from one arbitrary obstacle point, the search is operated towards both clockwise and anti-clockwise directions with maximal angle $\theta_{\text{thr}}$. An obstacle point is incorporated into the cluster when it is searched within $\theta_{\text{thr}}$, otherwise, the search is terminated and a new cluster is initialized with an unlabelled obstacle point.

The above search process is continued until all the obstacle points are assigned with corresponding clusters. The clusters containing too few points are dropped off. For each cluster, its boundary is the first and the endpoint during the search process.

#### 3.3.3 Height filter

The endpoint $\boldsymbol{p}$ is compared with road model $\boldsymbol{P}_{\text{road}}$, it will be added into the curb candidate set $\boldsymbol{P}_{\text{curb}}$, if its height is within a height threshold $h_{\text{thr}}$.

#### 3.3.4 Distance filter

The above algorithm attains high recall but poor accuracy since the false positive exists in the non-road areas. To eliminate false positive, a distance filter[7] is utilized for each layer. An example of distance filter is illustrated in Figure 5.

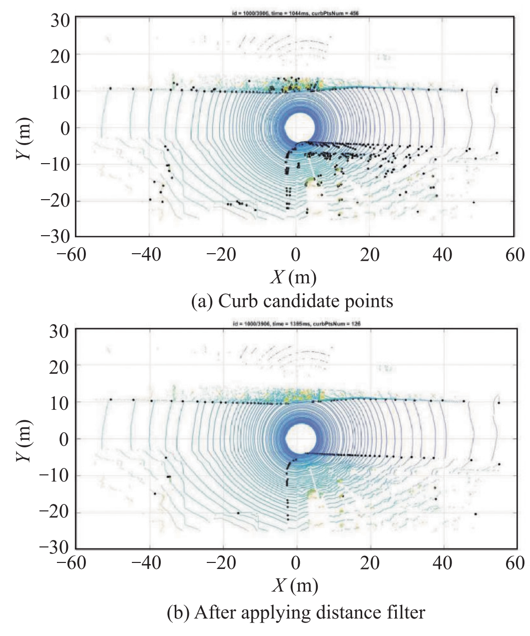


**Fig. 5 Curb candidates selctor**

## 4 Experimental results

In this section, the proposed curb detection and localization algorithm are validated in real traffic scenes, also the proposed algorithms are compared with other state-of-the-art algorithms.

The intelligent vehicle KUAFU-1st[13] is equipped with various sensors including a camera, LiDAR/radar, and GPS/IMU are equipped. Among them, the mode of GPS is RTK and gains positioning accuracy high than 0.1 m, which is adequately served as ground truth for localization. Two routes are recorded in Changshu city, China and named SUDOKU and HIGHWAY, respectively.

In order to validate the efficacy of the proposed curb detection algorithm, several state-of-the-art algorithms are implemented. For Reference [6], the ground is first estimated by RANSAC with plane-fitting tolerance of 0.3 m. Both References [7] and [12] use the parameter recommended in their own paper as the initial value and tuned for the best results for our collected SUDOKU and HIGHWAY datasets.

By empirical observation, curve fitting involved in References [7,12,10] requires discerning left and right direction for road curbs, which may be ambiguous in sophisticated intersections. Therefore, the curb fitting steps are dropped out and only detected curb points are reserved for comparison.

The results of the curb detection algorithm with regards to precision, recall, and F-value is listed in Table 1. Generally, the proposed algorithm is slightly good than other algorithms in the HIGHWAY dataset and much better than others in SUDOKU dataset. A detailed analysis is following.

**Table 1 Curb detection evaluation**

| | Metric | Our | ZHANG[6] | HATA[7] | CHEN[12] | OGM[10] |
|---|---|---|---|---|---|---|
| HIGHWAY | Precision | 0.693 0 | 0.701 1 | 0.584 1 | 0.596 6 | **0.715 4** |
| | Recall | **0.389 6** | 0.234 4 | 0.304 9 | 0.283 6 | 0.372 4 |
| | *F*-value | **0.496 5** | 0.349 5 | 0.398 8 | 0.381 5 | 0.487 3 |
| SUDOKU | Precision | **0.694 0** | 0.659 7 | 0.544 1 | 0.573 2 | 0.586 9 |
| | Recall | **0.545 5** | 0.432 4 | 0.465 4 | 0.420 8 | 0.416 9 |
| | *F*-value | **0.606 5** | 0.516 9 | 0.498 3 | 0.481 4 | 0.484 0 |

For the HIGHWAY dataset, traffic scenes are relatively clear, the road surface is mostly planar and the curbs are much higher than the road surface, ranging from 0.5 m to 1.0 m. All the features proposed like smoothness arc length[12], ring compression analysis[7], and spatial feature[6] are faded compared with height difference[10]. The precision of the proposed algorithm is a little worse than References [6, 10], but attains a higher recall and *F*-value among all the curb detection algorithms. This is reasonable because References [6, 10] explicitly detects road surfaces and detects curb points among obstacle points. Road modeling determines the performance of curb detection in relatively simple highway scenes. Our algorithm achieves the best *F*-value since its effective road surface modeling is better than References [6,10]. Besides better performance, our algorithm is also easy to deploy than OGM because no prestored vehicle trajectory is required. To further validate the proposed algorithm, the curb detection results are illustrated in Figure 6, where a density occlusion is presented in a highway scene. The green lines denote manually labeled HD curb maps, black points denote correctly detected curb points, and red points denote falsely detected curb points.

The SUDOKU dataset is much more challenging than HIGHWAY in several aspects. The first is that the road surface in SUDOKU is barely planar, and this is typical for urban traffic scenes. The curbs in SUDOKU is much lower and irregular, ranging from 0.05 m to 0.20 meter above the road surface. The second is an intersection in SUDOKU is complicated, but the importance of curbs in intersections becomes higher since urban scenes need stricter localization accuracy than highway scenes. From Table 1, we can infer that the proposed algorithms are much better than other algorithms with respect to precision, recall, and *F*-value. This indicates that our algorithm is suitable for urban scenes.

More specifically, HATA and CHEN produce quite a few false positive points. HATA's[7] algorithm is based on ring compression analysis, which requires an accurate sensor installation and planar road surface assumption. Features in CHEN[12] including the smoothness feature and smooth arc length feature can be easily failed when layer data is sparse over 30.0 meters. Similar to HATA, ZHANG[6] requires precise sensor installation. In addition, though the parameter thresholds have a clear physical concept in Reference [6], it seems that HDL-64E we employed is different from the HDL-32E which Zhang used. The data in each layer of HDL-64E are not configured with equal azimuth angle, and the distance accuracy is a little worse than HDL-32E's. For OGM[10], the physical accuracy of its detected curb points is heavily dependent on the cell's resolution in the occupancy

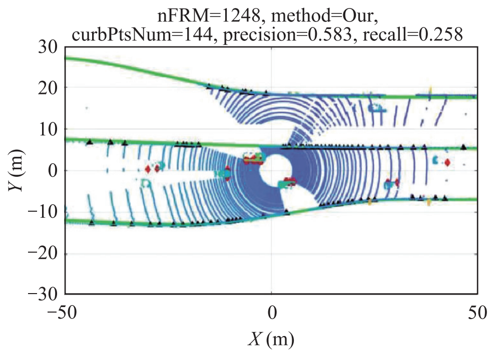


(a) The proposed method

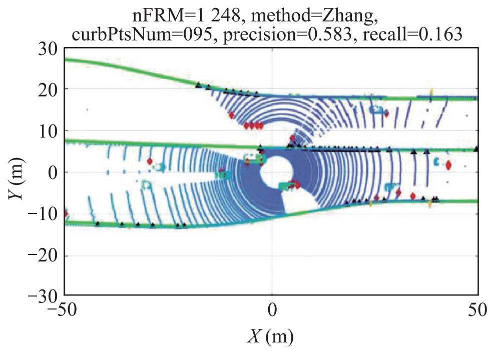


(b) ZHANG method[6]

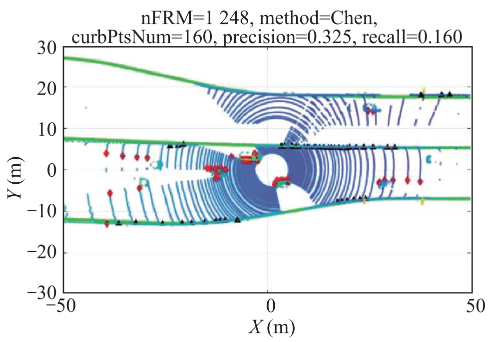


(c) CHEN method[12]

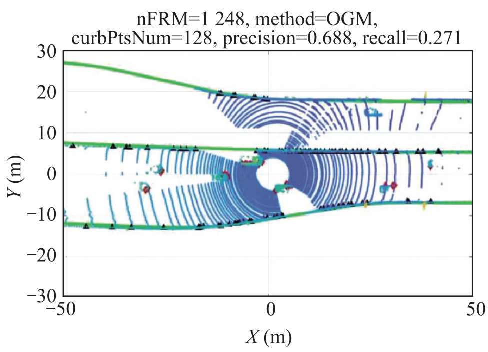


(d) OGM method[10]

**Fig. 6 Curb detection results for HIGHWAY**

grid map, therefore OGM is a viable choice for online curb detection but it is not suitable for precise curb map building.

## 5 Conclusion

In this paper, an efficient curb detection and mapping algorithm is proposed to attain precise curb shape under noise and outliers. Compared with traditional parameter estimation techniques, the proposed iGPR assumes no shape prior and requires less parameter tuning. In the experimental parts, two large-scale routes over 20 kilometers are elaborately presented. The proposed algorithm is compared with the state-of-the-art algorithms and achieves moderate improvements. The future work will focus on reliable multi-modal curb detection which fuses camera, radar, and HD map.

## Declaration of competing interest

The authors have no competing interests to declare that are relevant to the content of this article.

## References

[1] BAI D, CAO T, GUO J, et al. How to Build a Curb Dataset with Lidar Data for Autonomous Driving [C] //2022 International Conference on Robotics and Automation (ICRA). Philadelphia, USA: IEEE, 2022: 2576-2582.

[2] ROMERO L M, GUERRERO J A, ROMERO G. Road Curb Detection: a Historical Survey [J]. Sensors, 2021, 21 (21): 6952.

[3] GUO D, YANG G, QI B, et al. Curb Detection and Compensation Method for Autonomous Driving via a 3-D-LiDAR Sensor [J]. IEEE Sensors Journal, 2022, 22 (20): 19500-19512.

[4] JUNG Y, JEON M, KIM C, et al. Uncertainty-aware Fast Curb Detection Using Convolutional Networks in Point Clouds [C] //2021 IEEE International Conference on Robotics and Automation (ICRA). Xi'an, China: IEEE, 2021: 12882-12888.

[5] ZOU M, KAGEYAMA Y. Road Curb Detection Based on a Deep Learning Framework [C] //2023 IEEE 13th Annual Computing and Communication Workshop and Conference (CCWC). Las Vegas, USA: IEEE, 2023: 0259-0262.

[6] ZHANG Y, WANG J, WANG X, et al. Road-Segmentation-ased Curb Detection Method for Self-Driving via a 3D-lidar Sensor [J]. IEEE Transactions on Intelligent Transportation Systems, 2018, 19 (12): 3981-3991.

[7] HATA A Y, OSORIO F S, WOLF D F. Robust Curb Detection and Vehicle Localization in Urban Environments [C] //2014 IEEE Intelligent Vehicles Symposium Proceedings. Ypsilanti, USA: IEEE, 2014: 1257-1262.

[8] GALLAZZI B, CUDRANO P, FROSI M, et al. Clothoidal Mapping of Road Line Markings for Autonomous Driving High-Definition Maps [C] //2022 IEEE Intelligent Vehicles Symposium (IV). Aachen, Germany: IEEE, 2022: 1631-1638.

[9] XIONG H, ZHU T, LIU Y, et al. Road-Model-Based Road Boundary Extraction for High Definition Map via LIDAR [J]. IEEE Transactions on Intelligent Transportation Systems, 2022, 23 (10): 18456-18465.

[10] WANG D, XUE J, CUI D, et al. A Robust Submap-Based Road Shape Estimation via Iterative Gaussian Process Regression [C] //2017 IEEE Intelligent Vehicles Symposium (IV). Redondo Beach, USA: IEEE, 2017: 1776-1781.

[11] WANG Y, WANG Z, HAN K, et al. Gaussian Process-Based Personalized Adaptive Cruise Control [J]. IEEE Transactions on Intelligent Transportation Systems, 2022, 23 (11): 21178-21189.

[12] CHEN T, DAI B, LIU D, et al. Velodyne-based Curb Detection up to 50 Meters Away [C] //2015 IEEE Intelligent Vehicles Symposium (IV). Seoul, South Korea: IEEE, 2015: 241-248.

[13] TAO Z, XUE J, WANG D, et al. An Adaptive Invariant EKF for Map-aided Localization Using 3D Point Cloud [J]. IEEE Transactions on Intelligent Transportation Systems, 2022, 23 (12): 24057-24070.